

Static elasticity of cordierite I: Effect of heavy ion irradiation on the compressibility of hydrous cordierite

R. Miletich · K. S. Scheidl · M. Schmitt · A. P. Moissl ·
T. Pippinger · G. D. Gatta · B. Schuster · C. Trautmann

Received: 18 December 2013 / Accepted: 24 March 2014 / Published online: 8 April 2014
© Springer-Verlag Berlin Heidelberg 2014

Abstract The effect of ion beam irradiations on the elastic properties of hydrous cordierite was investigated by means of Raman and X-ray diffraction experiments. Oriented single crystals were exposed to swift heavy ions (Au, Bi) of various specific energies (10.0–11.1 MeV/u and 80 MeV/u), applying fluences up to 5×10^{13} ions/cm². The determination of unit-cell constants yields a volume strain of 3.4×10^{-3} up to the maximum fluence, which corresponds to a compression of non-irradiated cordierite at $\sim 480 \pm 10$ MPa. The unit-cell contraction is anisotropic ($e_1 = 1.4 \pm 0.1 \times 10^{-3}$, $e_2 = 1.5 \pm 0.1 \times 10^{-3}$, and $e_3 = 7 \pm 1 \times 10^{-4}$) with the *c*-axis to shrink only half as much as the axes within the *ab*-plane. The lattice elasticity for irradiated cordierite ($\phi = 1 \times 10^{12}$ ions/cm²) was determined from single-crystal XRD measurements in the diamond anvil cell. The fitted third-order Birch–Murnaghan

equation-of-state parameters of irradiated cordierite ($V_0 = 1548.41 \pm 0.16 \text{ \AA}^3$, $K_0 = 117.1 \pm 1.1$ GPa, $\partial K/\partial P = -0.6 \pm 0.3$) reveal a 10–11 % higher compressibility compared to non-irradiated cordierite. While the higher compressibility is attributed to the previously reported irradiation-induced loss of extra-framework H₂O, the anomalous elasticity as expressed by elastic softening (β_a^{-1} , β_b^{-1} , $\beta_c^{-1} = 397 \pm 9$, 395 ± 28 , 308 ± 11 GPa, $\partial(\beta^{-1})/\partial P = -4.5 \pm 2.7$, -6.6 ± 8.4 , -5.4 ± 3.0) appears to be related to the framework stability and to be independent of the water content in the channels and thus of the ion beam exposure.

Keywords Cordierite · Heavy-ion irradiation · High-pressure Raman spectroscopy · Single-crystal diffraction · Equation of state · Static compressibility

R. Miletich · K. S. Scheidl (✉) · T. Pippinger
Institut für Mineralogie und Kristallographie, Universität Wien,
Althanstrasse 14, 1090 Vienna, Austria
e-mail: katharina.sarah.scheidl@univie.ac.at

M. Schmitt · A. P. Moissl
Institut für Geowissenschaften, Universität Heidelberg,
Im Neuenheimer Feld 234-236, 69120 Heidelberg, Germany

Present Address:
M. Schmitt
Institut für Allgemeine, Anorganische und Theoretische Chemie,
Universität Innsbruck, Innrain 80-82, 6020 Innsbruck, Austria

Present Address:
A. P. Moissl
Institut für Angewandte Geowissenschaften, Technische
Universität Darmstadt, Schnittspahnstrasse 9, 64287 Darmstadt,
Germany

G. D. Gatta
Dipartimento di Scienze della Terra, Università degli Studi di
Milano, Via Botticelli 23, 20133 Milan, Italy

B. Schuster · C. Trautmann
GSI Helmholtzzentrum für Schwerionenforschung,
Planckstrasse 1, 64291 Darmstadt, Germany

B. Schuster · C. Trautmann
Material- und Geowissenschaften, Technische Universität
Darmstadt, Alarich-Weiss-Str. 4, 64287 Darmstadt, Germany

B. Schuster
Institut für Festkörperphysik, Technische Universität Darmstadt,
Hochschulstrasse 6-8, 64289 Darmstadt, Germany

Present Address:
B. Schuster
Areva GmbH, Paul-Gossen-Str. 100, 91052 Erlangen, Germany

Introduction

The structure–property relationship of cordierite, the magnesium iron aluminum silicate $(\text{Mg,Fe})_2\text{Al}_4\text{Si}_5\text{O}_{18}$ in a simplified form, has received considerable attention as a mineral and ceramic component because of its exceptional physical properties, which are of great interest for various industrial applications (e.g., Camerucci et al. 2001). This includes the remarkable ability to sustain large temperature gradients and temperature changes on a short timescale and thermomechanical properties related to low thermal volume expansion (e.g., Hochella et al. 1979; Mirwald 1981; Ikawa et al. 1986; Haussühl et al. 2011). The cordierite structure is apparently stable over a broad pressure and temperature range and is known, in particular at high-temperature conditions, to substitute various trace elements and variable amounts of volatiles (e.g., Bertoldi et al. 2004 and references therein). In geoscience, cordierite is used as a geothermobarometer and for monitoring paleofluid compositions (e.g., Bhattacharya 1986; Harley et al. 2002; Bul'bak and Shvedenkov 2005). Structural changes and related polymorphism are well known on temperature variations and originate from the Al, Si-order within the aluminosilicate framework, as manifested by a symmetry change from ordered *Cccm* (=cordierite) to disordered *P6/mcc* (=indialite) space–group symmetry above the critical temperature of $\sim 1,750$ K (e.g., Putnis 1980a; Armbruster 1985a; Redfern et al. 1989; Daniels et al. 1994; Malcherek et al. 2001). Most recent experimental high-pressure studies suggest the pressure-induced overhydration of the orthorhombic structure above 4 GPa to take place without changes in the symmetry (Likhacheva et al. 2012, 2013), while above 6.9 GPa, cordierite transforms to a high-pressure polymorph of apparently triclinic symmetry (Miletich et al. 2014).

Recent investigations of the material structure at non-ambient conditions encompass experimental ion irradiation. Extensive investigations currently focused on material alterations related to ion beam exposure (Weikusat et al. 2008, 2010; Miletich et al. 2010), because of reported capability to sustain relatively high doses of irradiation and simultaneously showing only minor alterations on the structure. Irradiation experiments using relativistic heavy ions revealed the irradiation-induced dehydration of extra-framework H_2O contents and the speciation change in trace oxocarbon channel constituents, i.e., the formation of molecular carbon monoxide (Weikusat et al. 2008, 2010). Together with defect-associated charge transfers related to the irradiation-induced formation of ferric iron, which is macroscopically evidenced by the typical radio-coloration (Nasdala et al. 2006), the subtle changes in the molecular species inside the channels are the only verifiable alterations. The structure apparently preserves the crystalline state and its crystallographic long-range order up to

relatively high fluences without any indication for a typical irradiation-induced degradation of the long-range order as observed for many other minerals such as mica (Vetter et al. 1998), quartz (Ramos et al. 2000; Afra et al. 2013), or apatite (Miro et al. 2005). Raman investigations by line scans across the interface of irradiated and non-irradiated crystal domains provide clear evidence for strain and strain gradients due to an obvious size mismatch of crystalline domains, showing gradients scaling with the irradiation dose (Weikusat et al. 2010).

In the context of systematic investigations on the elastic behavior of cordierite material under various conditions (Miletich et al. 2014), this work presents effects of ion irradiation-induced structural alterations on elastic properties with particular focus on (1) the effect of irradiation on the unit-cell parameters; (2) the effect of crystal orientation and anisotropy with respect to the ion beam direction and the changes in individual lattice directions; and (3) irradiation effects on the isothermal compression behavior at room temperature (RT). We report in situ high-pressure measurements on single crystals in diamond anvil cells (DACs) analyzed by means of X-ray diffraction (XRD) and micro-Raman spectroscopy. All investigations were carried out on pristine untreated and artificially irradiated crystal specimens.

Experimental

Sample material and cordierite specimen

Material used in this study was single crystals of natural, untreated hydrous low-sodium cordierite $(\text{Mg,Fe})_2\text{Al}_4\text{Si}_5\text{O}_{18}$ samples from Mount Tsilaizina/Madagascar. The two sample specimens “Tsi1” and “CORTS” with $X_{\text{Fe}} \approx 12\%$, 0.7–0.9 wt% H_2O , and <0.4 wt% CO_2 are characterized by Miletich et al. (2010) and Weikusat et al. (2010). Compositions were analyzed for inhomogeneities by energy-dispersive X-ray analyses, and volatile contents were derived from relative intensities of vibrational modes in Raman spectra, following the method of Kaindl et al. (2006) and Haefeker et al. (2013). Crystal orientation (according to the crystallographic setting $a \sim 17.07$ Å, $b \sim 9.72$, and $c \sim 9.35$ Å) was provided by means of polarized microscopy and conventional X-ray film techniques (oscillation photographs) and through positioning according to the orientation matrices determined on a four-circle diffractometer. Double-sided polished crystal platelets with $\sim 3 \times 3$ mm² lateral dimensions were prepared from thin sections perpendicular to the oriented crystallographic axis. Sample denotations *_an*, *_ai*, *_bi*, *_bn*, *_ci*, and *_cn* correspond to the orientation (suffixes a, b, and c) and the irradiation state (n = not irradiated and i = irradiated). The

Table 1 Cordierite sample crystals, their orientation, and the beam parameters for different irradiation experiments with ^{197}Au and ^{209}Bi ions

Sample	Orientation cut \perp	Thickness (μm)	Ion	Energy (MeV/u)	Fluence ϕ (ions/cm 2)	Measurements
UNILAC irradiation						
Tsi1_ai	<i>a</i> -axis	80 ± 3	Au	11.1	1.0×10^{12}	HP-R
Tsi1_bi	<i>b</i> -axis	75 ± 3	Au	11.1	1.0×10^{12}	XRD, HP-R
Tsi1_ci	<i>c</i> -axis	60 ± 3	Au	11.1	1.0×10^{12}	HP-R
UNILAC irradiation						
Tsi1_bi(1e11)	<i>b</i> -axis	78 ± 3	Au	10.0	1.0×10^{11}	XRD
Tsi1_bi(5e11)	<i>b</i> -axis	86 ± 3	Au	10.0	5.0×10^{11}	XRD
Tsi1_bi(1e12)	<i>b</i> -axis	92 ± 3	Au	10.0	1.0×10^{12}	XRD
Tsi1_bi(5e12) ^a	<i>b</i> -axis	–	Au	10.0	5.0×10^{12}	–
Tsi1_bi(1e13)	<i>b</i> -axis	71 ± 3	Au	10.0	1.0×10^{13}	XRD
Tsi1_bi(5e13)	<i>b</i> -axis	61 ± 3	Au	10.0	5.0×10^{13}	XRD
SIS irradiation						
Tsi1_ai(SIS)	<i>a</i> -axis	520 ± 5	Au, Bi ^b	180	1.3×10^{12}	XRD
Tsi1_bi(SIS)	<i>b</i> -axis	560 ± 5	Au, Bi ^b	180	1.3×10^{12}	XRD
Tsi1_ci(SIS)	<i>c</i> -axis	550 ± 5	Au, Bi ^b	180	1.3×10^{12}	XRD

HP-R high-pressure Raman spectroscopy, XRD single-crystal X-ray diffraction

^a Sample lost after the irradiation experiment

^b Given by beam time limitations at the SIS, the fluence was accumulated in two different irradiation runs, first using Au ions up to 5×10^{11} ions/cm 2 followed by Bi ions

thickness and orientation of the different samples together with the irradiation parameters are listed in Table 1.

Ion irradiation experiments

Specimens of oriented crystal platelets were exposed to relativistic heavy ions (^{197}Au , ^{209}Bi) at the UNILAC linear accelerator and the *Schwerionen Synchrotron (SIS)* of the GSI *Helmholtzzentrum für Schwerionenforschung* (Darmstadt, Germany). At the UNILAC facility, Au ions of 1,790 and 2,187 MeV total kinetic energy (respective specific energies of 10.0 and 11.1 MeV per nucleon (MeV/u)) were used. SIS beams consisted of 3.55 GeV Au ions and 3.76 GeV Bi ions (specific energy 180 MeV/u). All irradiations were carried out under normal beam incidence with respect to the oriented crystallographic faces of the sample. Crystals of several mm in size were directly glued on Al sample holder, while small crystals (<1 mm) were packed between two 10- μm -thick Al foils. All irradiation experiments were conducted at ambient temperature, applying fluences ϕ between 1×10^{11} and 5×10^{13} ions/cm 2 (Table 1). To avoid sample heating, the beam intensity was limited to about 10^8 ions/cm 2 s. Flux and fluence were controlled via a secondary electron transmission monitor (SEETRAM) calibrated with a standard Faraday cup. The range and energy loss of the ions in cordierite were calculated with the SRIM-2008 code (Ziegler et al. 1985). For samples exposed at the UNILAC, the mean energy loss of the Au ions is about 23 keV/nm varying by less than 20 %

within the crystals. For all irradiations, the ion range was sufficiently large to completely penetrate through the thin platelets ($\sim 90 \mu\text{m}$ at UNILAC, $\sim 560 \mu\text{m}$ at SIS) according to dE/dx calculated in analogy to Weikusat et al. (2010).

Determination of unit-cell parameters at ambient and high-pressure conditions

Unit-cell constants of single crystals for both ambient and high-pressure samples were measured with a Stoe AED2 or Huber 5042 four-circle diffractometer using non-monochromatized Mo radiation from a sealed-tube source. The angles of diffracted Bragg peaks were recorded using diffractometer setting as reported by Hejny et al. (2012) and by employing fitting procedures as implemented in the SINGLE software (Angel and Finger 2011). Symmetry-constrained vector-least-square refinements were carried out to obtain precise lattice parameters. The high-pressure measurements were taken in the range between 10^{-4} and 6.62 GPa at room temperature on sample Tsi1_bi (irradiated at $\phi = 1 \times 10^{12}$ $^{197}\text{Au}/\text{cm}^2$). The results of static compression were determined from two experimental loadings (run A and run B, respectively) carried out with an ETH-type (Miletich et al. 1999, 2000) DAC (~ 0.1 -ct type Ia standard anvils; 0.6 mm culet face diameter; anvils mounted on 4-mm-thick polycrystalline Be backing plates). Both loadings were carried out using stainless steel gaskets (material type 1.4310), preindented from initial 250 μm to a starting thickness of 140 ± 5 (run A) and $105 \pm 5 \mu\text{m}$

(run B). Sample crystals (size $180 \times 75 \times 75 \mu\text{m}^3$ in run A, $100 \times 75 \times 40 \mu\text{m}^3$ in run B) were loaded together with an equally sized quartz standard crystal in y-cut orientation into gasket boreholes ($\sim 250 \mu\text{m}$ in diameter) using liquefied argon as hydrostatically acting pressure medium. Pressures were adjusted by means of laser-induced fluorescence following the ruby scale (Mao et al. 1986), and precise pressure values were derived from the V/V_0 ratio of the unit-cell volumes of quartz (Angel et al. 1997). Data collection of run A yielded 7 data points and was terminated due to bridging of the $75\text{-}\mu\text{m}$ crystal specimen between the two diamond anvils at a pressure of ~ 5 GPa. To avoid this problem, the sample for run B was thus thinned down to $\sim 40 \mu\text{m}$ before loading. The second run provided additional 8 data points up to ~ 7 GPa. The isothermal bulk moduli and individual axial compressibility coefficients (K and β^{-1} , respectively) and its pressure derivative ($\partial K/\partial P$ and $\partial(\beta^{-1})/\partial P$, respectively), based on a third-order Birch–Murnaghan equation-of-state parameters, were obtained by fits using EosFit software (Angel 2000).

High-pressure Raman spectroscopy

In situ high-pressure Raman spectra were recorded from in total four oriented crystal samples (non-irradiated and irradiated (Tsi1_bi, Tsi1_ci, 11.1 MeV/u Au ions, 1×10^{12} ions/cm²)) cut perpendicular to the *b*-axis and *c*-axis. High-pressure sample loadings were performed with the same DAC type as described above using low-fluorescence anvils and Be backing plates with $\sim 12^\circ$ optical ports giving access into the pressure chamber. Sample crystals (bn: $130 \times 100 \times 55$, bi: $160 \times 100 \times 65$, cn: $140 \times 110 \times 70$, ci: $100 \times 80 \times 70$, all measures in μm) were loaded into boreholes ($260\text{--}270 \mu\text{m}$ diameter, $135\text{--}140 \mu\text{m}$ thickness) of preindented steel gaskets. Pairs of samples of the same orientation were loaded together with small ruby spheres (Chervin et al. 2002) in one borehole using cryogenically liquefied argon. Luminescence spectra of ruby were used for pressure calibration, and considering uncertainties in the determination of line shifts, the values for derived pressures are within ± 0.05 GPa. In addition to reference spectra at 1 bar outside the DAC, a series of high-pressure spectra was recorded at $P = 0.32, 1.06, 2.53, 3.12, 4.41, 5.36$, and 5.76 GPa (samples cn and ci) and at $P = 1.69, 3.18, 4.32, 5.16$, and 5.90 GPa (samples bn and bi). All spectra were measured in 180° backscattering geometry on a Jobin–Yvon HR800 confocal spectrometer equipped with an OLYMPUS BXFM-ILHS optical microscope with the instrumental setting and calibration described by Weikusat et al. (2010), i.e., a grating with 1800 grooves per mm, a notch holographic filter, and a Peltier-cooled charge-coupled device (CCD) detector ($1,024 \times 256$

pixels, $26 \mu\text{m}$ in size). The spectra were excited using the 632.817 nm line of a He–Ne laser operated at 20 mW. A $50\times$ long working distance objective (numerical aperture 0.70, free working distance $\sim 10 \text{ mm}$) was used for laser beam focusing, allowing a lateral resolution of $\sim 2 \mu\text{m}$ and a spectral resolution of 0.8 cm^{-1} . All spectra were recorded with accumulation times of 1 s for the Rayleigh and neon lamp lines, 3 s for the ruby *R* lines, and 180 s per interval for the cordierite Raman spectra. The wave number accuracy was better than 0.5 cm^{-1} , and the spectral resolution was determined at $\sim 2 \text{ cm}^{-1}$. Fitting was done assuming Voigt band shapes using a freeware version of FITYK (fityk.nieto.pl). Resulting band positions at different pressures are listed in Tables 4 and 5.

Results and discussion

Irradiation-induced unit-cell contraction

Previous experimental studies on hydrous cordierite samples irradiated by swift heavy ions give clear evidence of strain across the interface between irradiated and non-irradiated domains (Weikusat et al. 2010). The evolution of cracks and the line shifts of Raman modes according to tensile stress across the interfaces indicates the obvious size mismatch of crystalline domains. Ion beam-induced amorphization typically leads to an expansion of the unit cell (e.g., Schouwink et al. 2010) in contrast to the here observed contraction of the cordierite unit cell (Miletich et al. 2010). Despite the fact that at higher fluences, cordierite becomes amorphous, this does not lead to a volume contraction. Therefore, the governing mechanism seems to be the ion-induced loss of water leading to a unit-cell contraction instead of amorphization-caused unit-cell expansion. Also, the defects accumulation which increases linearly with fluence is irrelevant compared to the loss of water molecules due to ion irradiation. Analyzing Raman shifts, line broadening, and the distribution of the luminescence background, depth profiles revealed gradients extending across approximately $30 \mu\text{m}$ around the stopping range of the ions. The strain gradients seem to scale with the degree of the irradiation damage and thus with the energy loss of the projectiles along their trajectory. Due to the gradients within the crystals, this earlier study did not allow to deduce lattice contraction data and anisotropies of high accuracy (Miletich et al. 2010). To minimize the occurrence of gradients, we therefore focus in this work on crystals homogeneously irradiated throughout the entire sample. The analysis includes three thick cordierite specimen (sample Tsi1) completely through irradiated at the SIS (180 MeV/u) as well as thin platelets exposed at the UNILAC (11.1 MeV/u).

Table 2 Lattice parameters a , b , and c and unit-cell volume as a function of the fluence ϕ (ions/cm²) for oriented crystal specimen irradiated along the crystallographic a -axis, b -axis, or c -axis; distortion parameter $\Delta = 1.094 (a - \sqrt{3}b)$ after Selkregg and Bloss (1980)

Sample	ϕ (ions/cm ²)	a (Å)	b (Å)	c (Å)	V (Å ³)	Δ
Crystal irradiated//[100]						
CORTS_an	0	17.0700 (12)	9.7253 (4)	9.3441 (5)	1551.22 (15)	0.2464
CORTS_ai(6e11)	6.0×10^{11}	17.0594 (8)	9.7176 (7)	9.3408 (8)	1548.48 (16)	0.2495
Tsi1_ai(SIS)	1.3×10^{12}	17.0450 (7)	9.7111 (7)	9.3397 (8)	1545.96 (15)	0.2460
Crystal irradiated//[010]						
CORTS_bn	0	17.0679 (7)	9.7242 (8)	9.3478 (8)	1551.47 (16)	0.2463
CORTS_bi(6e11)	6.0×10^{11}	17.0607 (11)	9.7181 (11)	9.3388 (12)	1548.35 (26)	0.2499
Tsi1_bi(1e11)	1.0×10^{11}	17.0636 (7)	9.7215 (5)	9.3473 (5)	1550.57 (9)	0.2467
Tsi1_bi(5e11)	5.0×10^{11}	17.0582 (5)	9.7176 (4)	9.3448 (4)	1549.03 (8)	0.2481
Tsi1_bi(1e12)	1.0×10^{12}	17.0501 (4)	9.7132 (4)	9.3420 (4)	1547.14 (9)	0.2476
Tsi1_bi(SIS)	1.3×10^{12}	17.0440 (7)	9.7105 (7)	9.3411 (8)	1546.01 (15)	0.2460
Tsi1_bi(1e13)	1.0×10^{13}	No Bragg intensities detected				
Tsi1_bi(5e13)	5.0×10^{13}	No Bragg intensities detected				
Crystal irradiated//[001]						
CORTS_cn	0	17.0693 (8)	9.7253 (7)	9.3451 (7)	1551.33 (16)	0.2457
CORTS_ci(6e11)	6.0×10^{11}	17.0549 (17)	9.7158 (23)	9.3403 (40)	1547.71 (53)	0.2479
Tsi1_ci(SIS)	1.3×10^{12}	17.0449 (8)	9.7104 (7)	9.3402 (8)	1545.92 (15)	0.2472

Given by the homogeneous exposure conditions, the determined lattice dimensions show high accuracy with uncertainties of the individual base vectors in the order of $<6 \times 10^{-5}$. The values for the unit-cell parameters and their precisions are comparable to values reported earlier for non-irradiated samples (e.g., Ullrich et al. 2009; Hejny et al. 2012; Miletich et al. 2014). Table 2 lists the measurements at 1 bar of samples exposed to various ion fluences. All lattice dimensions (a , b , c , V) decrease linearly as a function of the fluence (Fig. 1). Differentiating between the directions of the irradiation vector, i.e., the ion beam being parallel to the crystallographic principle axis perpendicular to the faces of the individual crystal plates, there is no detectable orientation effect observed with the degree of unit-cell contraction depending only on the fluence but not on the orientation of the sample relative to the ion beam (Fig. 2). On the other hand, the data yield a clear anisotropy observable for the degree of irradiation-induced contraction in different lattice directions, which is approximately twice as large for the a -axis and b -axis compared to that of the c -axis. While the earlier study based on only three samples (Miletich et al. 2010) assumed quasi-isotropic lattice contraction, the fluence series of this investigation clearly indicates anisotropic behavior (Fig. 2). This anisotropy is explained by the loss of H₂O molecules during irradiation and hence shrinking of the channels. Linear fits to the changes in the lattice dimensions up to fluences of $\phi = 1.3 \times 10^{12}$ ions/cm² yield a compressive strain of respective $\sim 1.4 \pm 0.1 \times 10^{-3}$ and $\sim 1.5 \pm 0.1 \times 10^{-3}$ for the a -axis and b -axis, while it is only $\sim 7 \pm 1 \times 10^{-4}$ for the c -axis. The analyses did not consider the obvious

outlier for sample CORTS_ci(6e11), having 4–5 times larger uncertainties compared to the other data points. The irradiation-induced lattice contraction is apparently isotropic within the ab -plane with no significant differences between the a -axis and b -axis directions. This explains why the distortion index ($\Delta = 1.094 (a - \sqrt{3}b)$) (Putnis 1980b; Selkregg and Bloss 1980) is independent of the ion fluence. This coincides with the known empirical relationship between the distortion index Δ and the H₂O content (Langer and Schreyer 1976), but is different from the finding of heat-treated cordierite, where Δ was found to be higher after thermal treatments at 900 °C (Malcherek et al. 2001). Strain originating from any thermal treatment is due to thermal expansion, indeed with values of opposite sign in most cases, but displaying an analogous anisotropy with the pronounced changes to occur within the ab -plane (cf. Malcherek et al. 2001).

According to the linear relationship shown in Fig. 1, the volume strain of $2.5 \pm 0.1 \times 10^{-3}$ at a fluence of 1×10^{12} ions/cm² can be extrapolated to $3.4 \pm 0.1 \times 10^{-3}$ at a fluence of $\phi = 1 \times 10^{13}$ ions/cm², which is in fair agreement with the value ~ 1.9 to 2.0×10^{-3} previously reported (Miletich et al. 2010). The difference in volume strain may be related to fluence uncertainties (10–20 %) when comparing different irradiation experiments.

While the same authors report that irradiated cordierite was not amorphized up to a fluence of 1×10^{13} ions/cm² on the same irradiation conditions with Au as ion projectiles, in the present study, the two samples exposed to the highest fluences (i.e., $\phi = 1 \times 10^{13}$ and 5×10^{13} ions/cm²) appear to be amorphous as evidenced by the lack of birefringence under crossed polarizers and the absence of any Bragg peak

Table 3 Lattice parameters a , b , and c and unit-cell volume V of sample Tsi1_bi (irradiated at $\phi = 1 \times 10^{12}$ $^{197}\text{Au}/\text{cm}^2$) for different pressures; pressures are derived from unit-cell volume of quartz after Angel et al. (1997); distortion parameter $\Delta = 1.094$ ($a - \sqrt{3}b$) after Selkregg and Bloss (1980)

No.	$V-Qz$ (\AA^3)	P (GPa)	a (\AA)	b (\AA)	c (\AA)	V (\AA^3)	Δ
A00	–	0.0001 ^a	17.0608 (21)	9.7166 (21)	9.3429 (20)	1548.78 (50)	0.2523
B08	–	0.0001 ^b	17.0576 (6)	9.7134 (8)	9.3443 (5)	1548.23 (15)	0.2554
A01	110.446 (12)	0.902 (5)	17.0218 (12)	9.6907 (27)	9.3169 (13)	1536.84 (49)	0.2587
A02	110.378 (10)	0.928 (4)	17.0213 (8)	9.6910 (16)	9.3163 (8)	1536.76 (29)	0.2582
A03	108.761 (12)	1.583 (5)	16.9917 (8)	9.6730 (16)	9.2954 (9)	1527.80 (30)	0.2599
B01	107.432 (19)	2.212 (10)	16.9667 (5)	9.6685 (11)	9.2771 (6)	1519.21 (15)	0.2411
B07	105.646 (19)	3.050 (10)	16.9250 (6)	9.6336 (10)	9.2501 (5)	1508.21 (15)	0.2616
A04	105.293 (12)	3.229 (6)	16.9180 (17)	9.6278 (36)	9.2431 (18)	1505.53 (65)	0.2645
B02	103.909 (18)	3.994 (9)	16.8833 (5)	9.6121 (11)	9.2167 (5)	1495.73 (14)	0.2567
A05	103.742 (10)	4.085 (6)	16.8701 (23)	9.6038 (47)	9.2110 (23)	1492.33 (83)	0.2575
B03	103.729 (19)	4.092 (10)	16.8780 (6)	9.6108 (11)	9.2127 (6)	1494.40 (15)	0.2534
A06	102.995 (17)	4.527 (10)	16.8611 (34)	9.5926 (63)	9.2010 (29)	1488.17 (1.09)	0.2685
B04	101.753 (20)	5.550 (12)	16.8124 (7)	9.5659 (15)	9.1740 (7)	1475.41 (18)	0.2669
B06	100.949 (18)	5.852 (9)	16.8012 (8)	9.5686 (14)	9.1508 (7)	1471.12 (16)	0.2493
B05	99.876 (20)	6.613 (12)	Not determined ^c				

^a At 1 bar, crystal mounted on glass fiber

^b At 1 bar, crystal mounted in DAC without pressure medium

^c Crystal with multidomain twinning corresponding to the reported triclinic high-pressure phase

Table 4 Fitted positions of selected Raman bands and their uncertainties (values in cm^{-1}) obtained for non-irradiated (“n”, first line) and irradiated (“i”, second line) crystal sections// (001) ; the irradiation was performed at 1×10^{12} ions/ cm^2

Band assignment (after Kaindl et al. 2011)		Pressure (GPa)							
		0.0001	0.32 (5)	1.06 (5)	2.53 (5)	3.12 (5)	4.41 (5)	5.36 (5)	5.76 (5)
b(T_21, T_23)	n:	121.92 (3)	n.d.	n.d.	117.41 (1)	115.39 (11)	112.92 (13)	110.05 (26)	109.92 (23)
	i:	n.d.	121.88 (11)	n.d.	121.79 (8)	n.d.	125.87 (51)	125.56 (26)	125.31 (19)
o(T_11) + b(T_16) + b(T_21, T_23)	n:	158.55 (6)	n.d.	n.d.	152.25 (18)	149.35 (17)	148.27 (37)	148.21 (42)	142.24 (52)
	i:	n.d.	158.21 (3)	n.d.	158.28 (28)	151.65 (21)	148.27 (37)	n.d.	158.70 (6)
b(M) + o(T_11)	n:	239.29 (3)	n.d.	239.61 (18)	241.40 (25)	241.24 (29)	241.43 (28)	241.38 (28)	241.28 (33)
	i:	n.d.	239.84 (17)	239.61 (20)	239.66 (14)	n.d.	n.d.	n.d.	n.d.
b(M)	n:	260.32 (3)	n.d.	259.76 (18)	259.53 (18)	258.79 (23)	258.90 (27)	258.86 (39)	259.33 (26)
	i:	n.d.	260.57 (19)	259.75 (22)	260.09 (13)	259.53 (26)	259.01 (21)	260.08 (19)	259.27 (19)
b(T_11, T_23) + b(T_21, T_23, T_26) + b(T_11, T_23) + o(M, T_16)	n:	294.72 (2)	n.d.	n.d.	296.14 (7)	295.87 (8)	296.51 (9)	296.64 (21)	296.72 (10)
	i:	n.d.	295.25 (8)	n.d.	295.09 (10)	n.d.	n.d.	n.d.	298.23 (44)
b(T_26)	n:	428.82 (2)	n.d.	n.d.	432.95 (9)	433.69 (11)	436.33 (14)	438.55 (25)	439.61 (15)
	i:	n.d.	428.94 (92)	n.d.	428.74 (13)	378.80 (92)	n.d.	n.d.	420.94 (92)
s(T_26, M) + b(T_16, T_26)	n:	555.24 (5)	n.d.	560.36 (34)	565.53 (15)	567.84 (20)	573.04 (6)	576.13 (10)	577.68 (12)
	i:	n.d.	555.69 (22)	560.51 (41)	555.59 (17)	568.97 (30)	573.12 (18)	576.78 (14)	579.59 (14)
s(M)	n:	578.23 (16)	n.d.	582.73 (28)	590.46 (57)	592.10 (1.05)	596.93 (44)	n.d.	585.16 (44)
	i:	n.d.	578.21 (82)	582.40 (32)	578.61 (45)	n.d.	n.d.	599.75 (90)	605.18 (95)
s(T_11)	n:	671.43(3)	n.d.	n.d.	680.68 (13)	683.23 (16)	687.28 (24)	690.84 (36)	691.75 (29)
	i:	n.d.	671.82 (16)	n.d.	671.58 (17)	n.d.	n.d.	689.34 (48)	693.46 (41)
s(T_21, T_23)	n:	972.93 (4)	n.d.	978.00 (31)	989.16 (14)	993.14 (18)	1001.42 (21)	1006.73 (34)	1009.72 (46)
	i:	n.d.	974.10 (16)	978.97 (30)	973.76 (15)	999.99 (1.12)	1002.32 (39)	1008.05 (31)	1011.61 (32)

in diffraction patterns. Irradiation-induced degradation of the long-range order has been reported by Lee et al. (1986) under electron beam exposure and for 1.5 MeV/u Xe ions above a critical amorphization fluence of 7.7×10^{13} ions/ cm^2 at 298 K (Wang et al. 1998). Our findings show that

the long-range order of the cordierite structure is preserved up to a fluence of at least $\phi = 1.0 \times 10^{12}$ ions/ cm^2 , while irradiation damages corresponding to fluences above 10^{13} ions/ cm^2 result in apparent degradation of the crystalline state.

Table 5 Fitted band positions and their uncertainties (values in cm^{-1}) obtained from spectra of non-irradiated (“n”, first line) and irradiated (“i”, second line) crystal section//010

Band assignment (after Kaindl et al. 2011)	Pressure (GPa)					
		1.69 (5)	3.18 (5)	4.32 (5)	5.16 (5)	5.90 (5)
b(T ₂ 1,T ₂ 3)	n:	127.75 (11)	126.84 (13)	126.06 (7)	n.d.	n.d.
	i:	127.39 (21)	126.37 (13)	125.79 (8)	n.d.	n.d.
b(M) + o(T ₁ 1)	n:	240.11 (16)	240.76 (18)	241.56 (18)	n.d.	n.d.
	i:	239.30 (27)	240.40 (57)	n.d.	235.97 (1.33)	234.25 (1.14)
b(M)	n:	259.64 (4)	259.40 (3)	259.02 (4)	n.d.	266.05 (1.36)
	i:	259.56 (7)	259.24 (8)	258.93 (7)	262.87 (1.54)	261.22 (1.17)
b(M)	n:	368.04 (16)	371.23 (21)	371.03 (26)	n.d.	n.d.
	i:	367.58 (28)	359.13 (1.83)	329.48 (1.5)	329.35 (1.08)	330.72 (80)
s(T ₂ 6,M) + b(T ₁ 6,T ₂ 6)	n:	561.98 (13)	568.91 (10)	572.84 (10)	n.d.	n.d.
	i:	562.32 (28)	569.01 (21)	573.31 (20)	543.49 (1.74)	n.d.
s(M)	n:	585.22 (14)	592.51 (15)	597.23 (17)	n.d.	n.d.
	i:	585.36 (23)	593.37 (31)	599.38 (45)	n.d.	n.d.
s(T ₁ 1)	n:	677.49 (24)	683.27 (25)	687.06 (23)	680.85 (1.89)	n.d.
	i:	677.87 (46)	685.45 (59)	686.25 (58)	n.d.	n.d.
s(T ₂ 1,T ₂ 3)	n:	983.29 (8)	994.27 (7)	1000.53 (8)	n.d.	n.d.
	i:	983.57 (34)	994.59 (17)	1001.54 (19)	n.d.	952.01 (2.09)

Raman spectra of pressurized and ion-irradiated cordierite

Raman spectra at high pressures were recorded for four different *b*-axis- and *c*-axis-oriented samples, for both orientations with each one non-irradiated and irradiated specimen (samples bn, bi, cn, and ci). Fig. 3 shows the non-polarized spectra of non-irradiated (Fig. 3a) and irradiated (Fig. 3b) cordierite sections perpendicular to the *c*-axis at pressures up to 5.76 GPa. Argon was chosen as pressure-transmitting medium, although behaving quasi-hydrostatically (Angel et al. 2007), because both liquid and the solid phases of Ar are Raman inactive. Although being a component known as a potential channel constituent, Ar does not penetrate the structural channels on compression at RT conditions (Miletich et al. 2014); significant substitution was reported only on hydrothermal treatment (Armbruster 1985b).

Within the recorded range, the Raman spectra exhibit observable characteristic modes that compare well with measured and calculated spectra reported by McMillan et al. (1984), Kolesov and Geiger (2000), Geiger and Grams (2003), Nasdala et al. (2006), Weikusat et al. (2010), Kaindl et al. (2011), Likhacheva et al. (2012), and Haefeker et al. (2012, 2013). Spectra at pressures greater than ~6.5 GPa reveal a significant quality change showing much lower signal-to-background ratios and striking broadening of peaks. These changes correlate with the high-pressure phase transition reported recently (Miletich et al. 2014) and appear for non-irradiated and irradiated cordierite at 7.2 GPa. In the case of the high-pressure loading of the crystal specimens cut perpendicular to the *b*-axis, Raman

measurements recorded at pressures above 5 GPa reveal severe changes such as three times larger half widths and uncertainties in the band position up to $\pm 2 \text{ cm}^{-1}$. These features are attributed to strain gradients and deviatoric stress, which probably originate from the bridging of the sample crystals between the culet faces of the two diamond anvils. The quality of all recorded spectra is in general characterized by relatively high noise due to the geometrical restrictions for the optical access to the pressure chamber, as limited by the geometry of the optical port in the used Be backing plates.

Characteristic bands of significant intensities are attributed to vibrational modes following the band assignment given by Kaindl et al. (2011) reported for spectra of the Fe-free end member at 1 bar (see Tables 4, 5). Apart from these bands assigned to stretching and bending modes of the framework, all high-pressure Raman spectra show a weak band at $\sim 3,600 \text{ cm}^{-1}$ (not shown), which is ascribed to the O–H stretching mode of the molecular H₂O inside the channels (Kolesov and Geiger 2000; Kolesov 2006; Weikusat et al. 2008). The spectral characteristics of the assigned modes obtained from applied peak fitting procedures reveal reasonable values for the half widths ($< 0.8 \text{ cm}^{-1}$) and band position accuracy ($0.2\text{--}1.1 \text{ cm}^{-1}$) for all spectra recorded under quasi-hydrostatic conditions of the used pressure medium. Non-irradiated (bn, cn) and irradiated (bi, ci, $\phi = 1.0 \times 10^{12} \text{ ions/cm}^2$) samples of same orientation reveal remarkable differences in the quality of the spectra. The background of irradiated crystals is in general significantly higher due to the increased luminescence

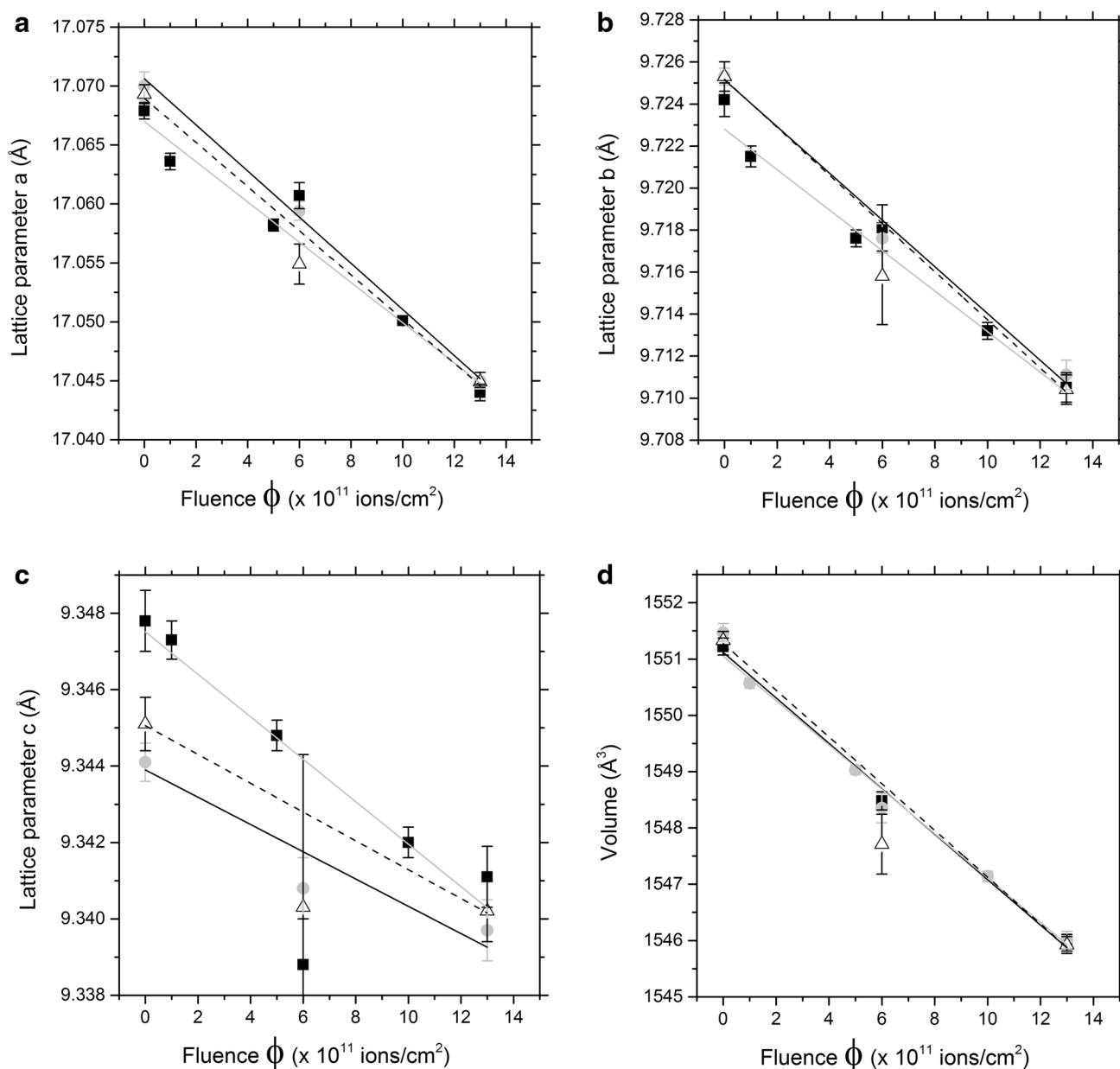


Fig. 1 Irradiation-induced lattice contraction as a function of the fluence ϕ of 2.2 GeV (11.1 MeV/u) Au ions between 0 and 1.3×10^{12} ions/cm²: **a** lattice parameter a ; **b** lattice parameter b ; **c** lattice param-

eter c ; and **d** unit-cell volume V ; orientations correspond to crystal plates // (100) (gray circles), // (010) (black squares), and // (001) (open triangles); lines correspond to weighted linear fits

(cf. Weikusat et al. 2008, 2010). This can be ascribed to the higher concentration of point defects produced by the ion beam (Nasdala et al. 2006; Miletich et al. 2010). A significant decrease can be confirmed for the O–H stretching band, which scales with the known irradiation-induced reduction in H₂O content. Compared to pristine samples, the full widths at half height of any of the observed vibrational modes of irradiated crystals show no or only a small increase.

A significant pressure dependency can be reported for the band position of individual modes showing a linear shift with increasing pressure (Fig. 4). The bands located at wave numbers >400 cm⁻¹ reveal in general the typical pressure-induced blueshift ($\partial\nu/\partial P > 0$) with positive values for $\partial\nu/\partial P$ between 3.4 and 6.4 cm⁻¹ GPa⁻¹. The position of the bands located between 200 and 400 cm⁻¹ appears to be independent on pressure ($\partial\nu/\partial P \approx 0$, i.e., +0.3 for ν_{241} , -0.2 for ν_{261} , -0.4 for ν_{297} in cm⁻¹ GPa⁻¹ units), while the

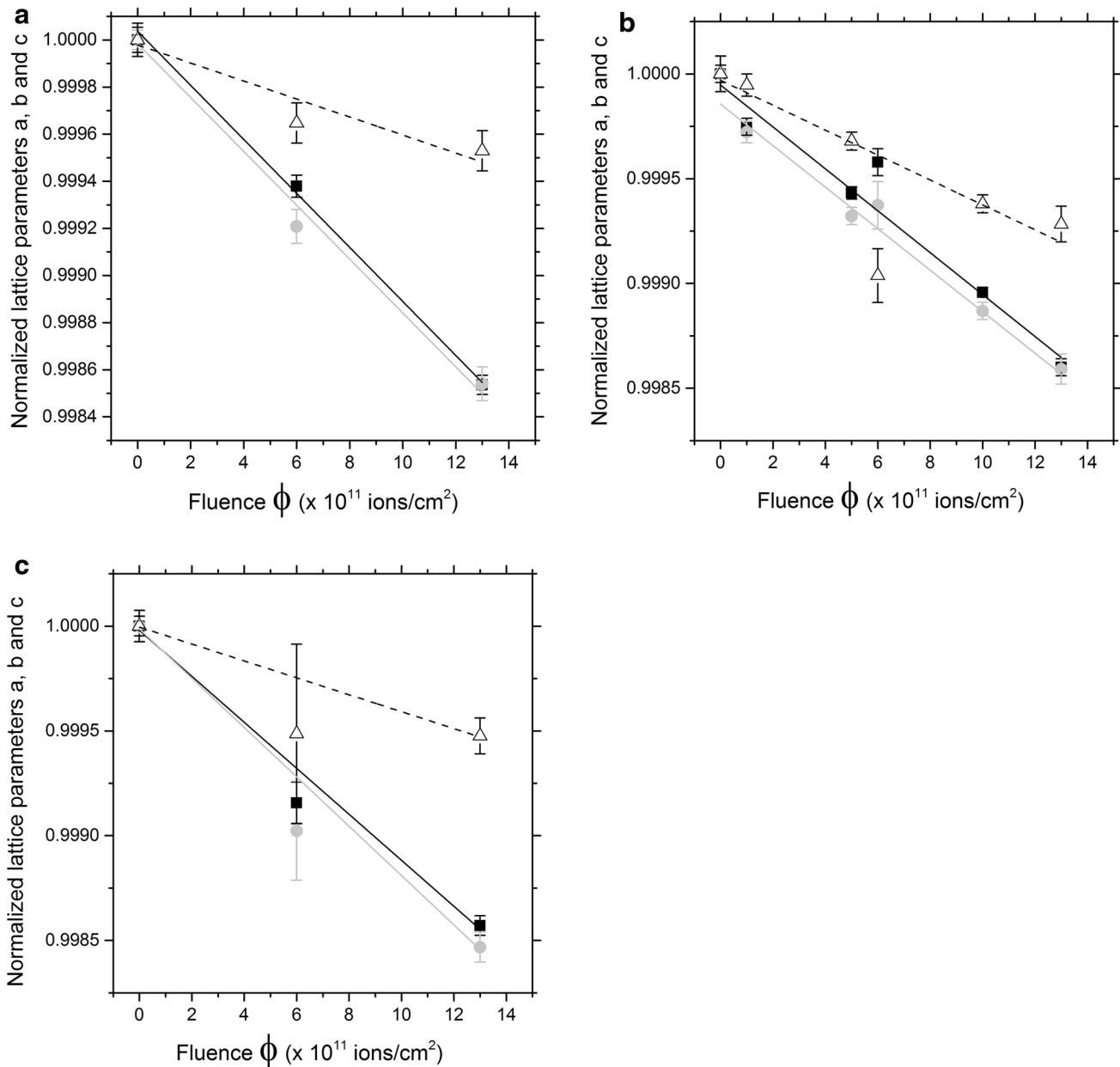


Fig. 2 Normalized lattice parameter a (black squares), b (gray circles), and c (open triangles) as a function of the fluence ϕ between 0 and 1.3×10^{12} ions/cm² in crystal plates of different orientations: **a**

(100) crystal plate (=sample ai); **b** (010) crystal plate (=sample bi); and **c** (001) crystal plate (=sample ci); lines correspond to weighted linear fits

two low-frequency lattice modes below 200 cm^{-1} $\partial\nu/\partial P$ show negative values (-2.8 for ν_{160} and $-2.1 \text{ cm}^{-1} \text{ GPa}^{-1}$ for ν_{120}). These observations are in good agreement with the findings reported by Likhacheva et al. (2012).

In the case of irradiated samples, the only differences compared to non-irradiated samples appear for the two low-frequency bands at 122 and 158 cm^{-1} related to translational and librational modes of larger framework units, respectively. While for the non-irradiated sample, $\partial\nu/\partial P$ of these two modes is negative, it changes to slightly positive

value ($+0.6 \text{ cm}^{-1} \text{ GPa}^{-1}$ for ν_{122} and $+0.1 \text{ cm}^{-1} \text{ GPa}^{-1}$ for ν_{158}) for the irradiated sample. As redshifts of modes in high-pressure spectra are indicative of tensile strain, the evolution of these lattice modes is probably related to the compressional anisotropy within the ab -plane. Since these modes are assigned to bending modes between tetrahedral units, this radiation-induced change might reflect the increasing diversification between the a -axis and b -axis, as exemplified by Miletich et al. (2014) showing the a -axis to stiffen up, while the b -axis undergoes elastic softening.

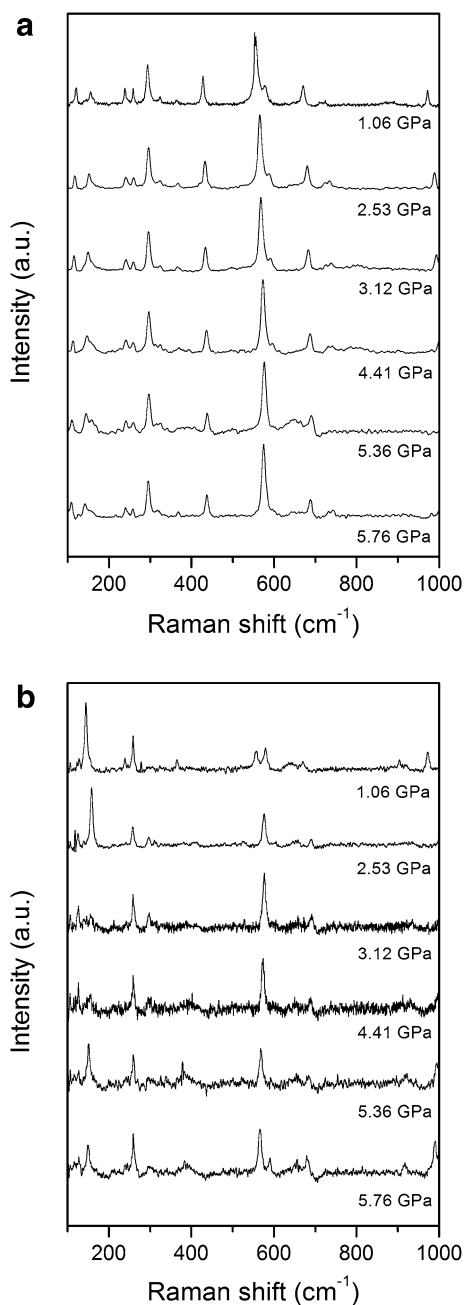


Fig. 3 High-pressure Raman spectra in the frequency range of 100 to 1,000 cm^{-1} of **a** non-irradiated crystal *cn* and **b** a crystal (*ci*) irradiated with 1×10^{12} ions/ cm^2 ; in all spectra, the background has been corrected, and additionally, the data were smoothed by the Savitzky–Golay method in order to reduce noise; the orientation of the *a*-axis and *b*-axis in reference to the E-vector for both samples was random, causing slightly different Raman spectra

Comparative equation-of-state measurements

The results of high-precision XRD measurements of sample Ts11_bi (irradiated at $\phi = 1 \times 10^{12}$ Au/ cm^2 , UNILAC irradiation) with respect to unit-cell edges and volumes on

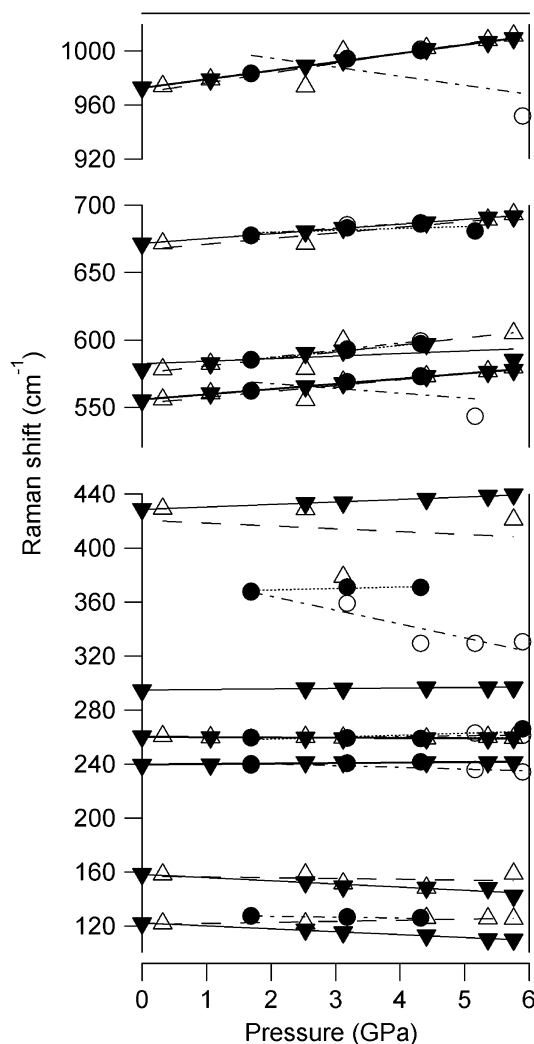


Fig. 4 Shift of selected Raman bands as a function of pressure for non-irradiated samples (*bn* (filled circle) and *cn* (filled triangle)) and samples irradiated with 1×10^{12} ions/ cm^2 (*bi* (open circle) and *ci* (open triangle)); the accuracy of the pressure measurements is within 0.05 GPa; lines correspond to the linear fits used to determine the change in band position with pressure ($\partial\nu/\partial P$)

static compression are summarized in Table 3. The irradiation caused slight peak broadening but does not impact the determination of unit-cell parameters. The evolution of *a*, *b*, *c*, and *V* as a function of pressure (hydrostatic compression in argon) is shown in Fig. 5a comparing the compressibility data of non-irradiated and irradiated hydrous cordierite below the critical pressure of the orthorhombic-to-triclinic phase transition at ~ 7 GPa (Miletich et al. 2014). Data points measured above 7 GPa are characterized by significant changes in the XRD Bragg peak profiles, which indicate metrical changes, the existence of more than one crystal domain, and the occurrence of structural gradients across domain boundary walls. Comparing the results of equation-of-state fits of the irradiated sample to the fitted

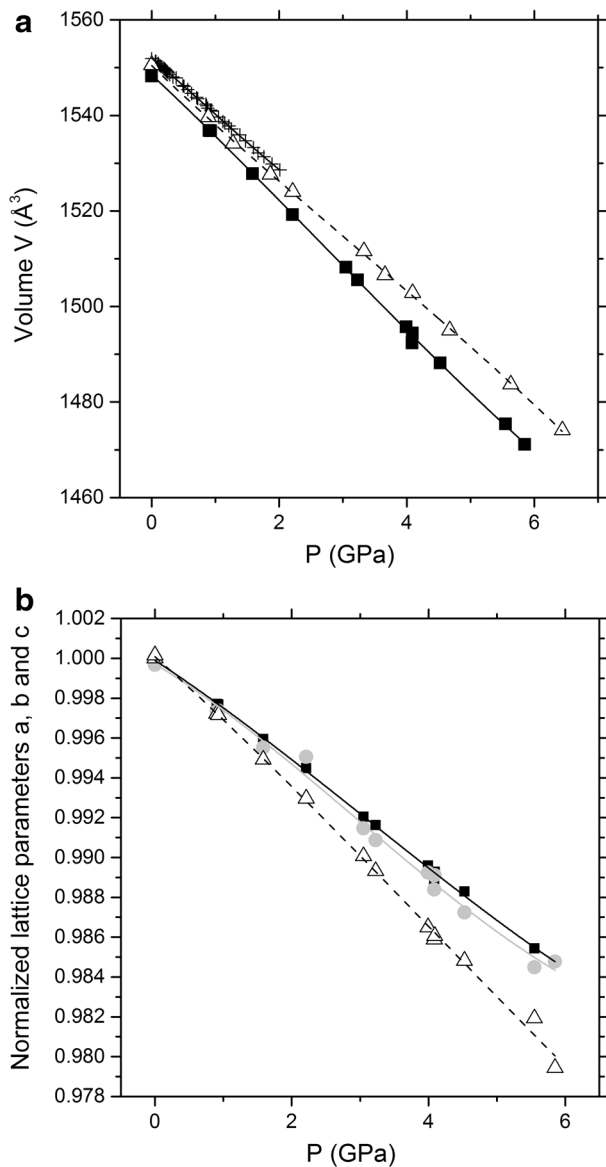


Fig. 5 Compression behavior of irradiated (*full symbols*) and non-irradiated (*open symbols*) Tsi1_bi (irradiated at $\phi = 1 \times 10^{12} \text{ }^{197}\text{Au/cm}^2$) cordierite samples between room pressure and 6 GPa. *Lines* represent the equations of state fitted to the datasets with the parameters given in Table 6; **a** unit-cell volume as a function of pressure, non-irradiated (*open triangles*) and irradiated (*black squares*) both compressed in argon, and non-irradiated compressed in H_2O (*plus signs*); **b** normalized lattice parameters a/a_0 (*black squares*), b/b_0 (*gray circle*), and c/c_0 (*open triangles*) plotted versus pressure

Table 6 Results of the fits for the pressure dependencies of the crystallographic axes and the unit-cell volumes to third-order Birch–Murnaghan equations of state obtained by fits using EosFit (Angel 2000) for sample Tsi1_bi (irradiated at $\phi = 1 \times 10^{12} \text{ }^{197}\text{Au/cm}^2$)

V (\AA^3); a, b, c (\AA)	K_0, β_1^{-1} (GPa)	$\partial K/\partial P, \partial(\beta_1^{-1})/\partial P$	χ_w^2	$P_{\text{obs}} - P_{\text{calc}}$ (GPa)
$V_0 = 1548.41$ (16)	$K_0 = 117.1$ (1.1)	$\partial K/\partial P = -0.6$ (0.3)	1.49	≤ 0.169
$a_0 = 17.0595$ (13)	$1/3 \beta_a^{-1} = 132.5$ (3.1)	$1/3 \partial(\beta_a^{-1})/\partial P = -1.5$ (0.9)	7.03	≤ 0.218
$b_0 = 9.7148$ (24)	$1/3 \beta_b^{-1} = 131.7$ (9.6)	$1/3 \partial(\beta_b^{-1})/\partial P = -2.2$ (2.8)	11.23	≤ 0.358
$c_0 = 9.3444$ (17)	$1/3 \beta_c^{-1} = 102.8$ (3.8)	$1/3 \partial(\beta_c^{-1})/\partial P = -1.8$ (1.0)	15.28	≤ 0.252

parameters of non-irradiated hydrous cordierite, the isothermal bulk moduli and its pressure derivative (based on a third-order Birch–Murnaghan equation-of-state fit) yield $K_{0,298} = 117.1 \pm 1.1$ GPa and $\partial K/\partial P = -0.6 \pm 0.3$ for compression at room temperature ($T = 298$ K). These values imply a higher compressibility of the irradiated sample relative to any non-irradiated one (i.e., 137.8 ± 1.5 GPa in H_2O , 127.7 ± 2.3 GPa in Ar, and 131.0 ± 1.3 GPa in methanol–ethanol, cf. Miletich et al. 2014).

The degree of compression for irradiated hydrous cordierite, which is about 10–11 % higher in comparison with the hydrous cordierite samples, can be attributed to the lower amount of H_2O inside the channels corresponding to the irradiation-induced dehydration (Weikusat et al. 2008, 2010; Miletich et al. 2010). Again, the result of this study provides evidence for the anomalous compressibility, as expressed by the value for $\partial K/\partial P$ being close to zero, which can be attributed to the elastic softening preceding the first-order transition at ~ 7 GPa. The compression data do not reveal any pressure-induced volume gain in analogy to the observed penetration of excess fluid components, as manifested by the overhydration effect reported by Likhacheva et al. (2013).

The compressional anisotropy is in analogy to that of non-irradiated samples with the a -axis and b -axis being less compressible than the c -axis (Fig. 5b). One remarkable difference is observed for the compression within the ab -plane, which is much more isotropic for the irradiated sample than for non-irradiated cordierite. The relative small differences in the compressibilities of the a -axis and b -axis do not develop into the pronounced diversification as described by Miletich et al. (2014) on approaching the critical transition. The similar behavior in axial compressibilities is not only restricted to low pressures up to 3 GPa, such as observed for non-irradiated cordierite, but can be extended to the highest pressure points of this study. Accordingly, the distortion index Δ (Putnis 1980b; Selkregg and Bloss 1980) appears to be independent on pressure. The absolute values for Δ are in the range of values observed for non-irradiated samples (i.e., 0.246–0.269) and do not provide any significant difference for the deviation from the pseudo-hexagonal metrics of the primitive subcell. The remarkable elastic softening effects with

significant negative $\partial(\beta^{-1})/\partial P$ coefficients are confirmed even to be expressed by the axial compressibilities, displaying equal $\partial(\beta^{-1})/\partial P$ coefficients for all three main axis, but all of them marginally negative or close to zero (Table 6).

Conclusions

Applying static high-pressure methods and high-precision measurements of lattice vectors allowed us to determine volume compression and the anisotropy of the elastic properties. The bulk modulus of the investigated sample exposed to 1×10^{12} Au ions/cm² was found to be 10–11 % smaller compared to any non-irradiated cordierite specimen. While the significantly higher compressibility is attributed to the previously reported irradiation-induced loss of extra-framework H₂O, the anomalous elasticity as expressed by elastic softening appears to be related to the framework stability independent of the exposure of the ion beam. The pressure derivative of the bulk modulus $\partial K/\partial P$, as well of the individual axial compressibility coefficients $\partial(\beta^{-1})/\partial P$, reveals equivalent behavior indicating the instability of the structure on approaching the critical pressure P_c of transformation at approximately 7 GPa. The experimental investigations by means of Raman spectroscopy and single-crystal X-ray diffraction yield evidence for a symmetry-breaking structural transition as observed in non-irradiated cordierite samples. Comparing the compression behavior between the non-irradiated and irradiated samples, the main striking feature of irradiated cordierite is the lack of the diversification between the compressibilities of the *a*-axis and *b*-axis on approaching P_c . This is manifested by the distortion index Δ to be zero within the experimental uncertainties independent on the pressure variations, while it was reported earlier to increase significantly at pressures above ~4 GPa. The quasi-isotropic behavior within the *ab*-plane direction might also be reflected by the redshift of low-frequency modes in the high-pressure Raman spectra to turn seemingly to a blueshift for the bending modes between tetrahedral framework units. Moreover, the precise determination of lattice parameters of crystals exposed to various ion fluences confirms irradiation-induced unit-cell contractions due to the removal of H₂O. The measurements revealed a volume strain of 3.4×10^{-3} up to the maximum fluence of 1.3×10^{12} ions/cm², which corresponds to an equivalent compression of non-irradiated cordierite at only ~480 ± 10 MPa. While the irradiation-induced unit-cell contraction was found to be anisotropic (in *c*-axis direction only half as large as within the *ab*-plane), a dependency on the direction of the ion beam relative to the crystal orientation is not observed. The extent of anisotropy for the irradiation-induced contraction is opposite to the

pressure-induced compressional anisotropy and is more like the anisotropy known from thermal expansion.

Acknowledgments We thank Gerald Giester and Herta Effenberger for their help to orient crystal specimens, Andreas Wagner and Ilona Fin for the careful preparation of crystal thin sections, Ilse Glass for performing EDX analyses, Angela Ullrich for carrying out individual XRD measurement on the CORTS sample, Christian Weikusat for his support with the Raman measurements at the GSI, and Pascal Schouwink for the technical assistance on the Huber diffractometer. Financial support within the scope of the BMBF-Verbundprojekt “Ioneninduzierte Strukturumbildung” (grant 05KK7VH1) is acknowledged. Finally, we thank the two reviewers for their valuable suggestions and great effort, which significantly improved the manuscript.

References

- Afra B, Rodriguez MD, Trautmann C, Pakarinen OH, Djurabekova F, Nordlund K, Bierschenk T, Giulian R, Ridgway MC, Rizza G, Kirby N, Toulemonde M, Kluth P (2013) SAXS investigations of the morphology of swift heavy ion tracks in α -quartz. *J Phys Condens Matter* 25:45006–45015. doi:10.1088/0953-8984/25/4/045006
- Angel RJ (2000) Equations of state. In: Hazen RM, Downs RT (eds) High-temperature and high-pressure crystal chemistry, *Rev Miner Geochem* 41:35–60
- Angel RJ, Finger LW (2011) Single: a program to control single-crystal diffractometers. *J Appl Crystallog* 44:247–251
- Angel RJ, Allan DR, Miletich R, Finger LW (1997) The use of quartz as an internal pressure standard in high pressure crystallography. *J Appl Crystallog* 30:461–466
- Angel RJ, Bujak M, Zhao J, Gatta GD, Jacobsen SJ (2007) Effective hydrostatic limits of pressure media for high-pressure crystallographic studies. *J Appl Crystallog* 40:26–32
- Armbruster T (1985a) Crystal structure refinement, Si, Al-ordering, and twinning in “pseudo-hexagonal” Mg-cordierite. *Neues Jahrbuch Miner Monatsh* 6:255–267
- Armbruster T (1985b) Ar, N₂, and CO₂ in the structural cavities of cordierite, and optical and X-ray single-crystal study. *Phys Chem Miner* 12:233–245
- Bertoldi C, Proyer A, Garbe-Schönberg D, Behrens H, Dachs E (2004) Comprehensive chemical analyses of natural cordierites: implications for exchange mechanisms. *Lithos* 78:389–409
- Bhattacharya A (1986) Some geobarometers involving cordierite in the FeO–Al₂O₃–SiO₂ (\pm H₂O) system: refinements, thermodynamic calibration, and applicability in granulite-facies rocks. *Contrib Mineral Petrol* 94:387–394
- Bul’bak TA, Shvedenkov GY (2005) Experimental study on incorporation of C-H-O-N fluid components in Mg-cordierite. *Eur J Miner* 17:829–838
- Camerucci MA, Urretavizcaya G, Castro MS, Cavalieri AL (2001) Electrical properties and thermal expansion of cordierite and cordierite-mullite materials. *J Eur Ceram Soc* 21:2917–2923
- Chervin JC, Canny B, Mancinelli M (2002) Ruby-spheres as pressure gauge for optically transparent high pressure cells. *High Pres Res* 21:305–314
- Daniels P, Wunder B, Sahl K, Schreyer W (1994) Changing lattice metrics of synthetic cordierites: the metastable hexagonal to orthorhombic transformation sequence during isothermal annealing. *Eur J Miner* 6:323–335
- Geiger CA, Grams M (2003) Cordierite IV: structural heterogeneity and energetics of Mg–Fe solid solutions. *Contrib Mineral Petrol* 145:752–764

- Haefeker U, Kaindl R, Tropper P (2012) Semi-quantitative determination of the Fe/Mg ratio in synthetic cordierite using Raman spectroscopy. *Am Miner* 97:1662–1669
- Haefeker U, Kaindl R, Tropper P (2013) Improved calibrations for Raman-spectroscopic determinations of CO₂ in cordierite using three excitation wavelengths (488, 515 and 633 nm). *Eur J Miner*. doi:10.1127/0935-1221/2013/0025-2276
- Harley SL, Thompson P, Hensen BJ, Buick IS (2002) Cordierite as a sensor of fluid conditions in high-grade metamorphism and crustal anatexis. *J Metamorph Geol* 20:71–86
- Hausühl E, Vinograd VL, Krenzel TF, Schreuer J, Wilson DJ, Ottlinger J (2011) High temperature elastic properties of Mg-cordierite: experimental studies and atomistic simulations. *Z Kristallogr* 226:236–253
- Hejny C, Miletich R, Jasser A, Schouwink P, Crichton W, Kahlenberg V (2012) Second order Pc2-P31c structural transition and structural crystallography of the cyclosilicate benitoite, BaTi₃Si₃O₉, at high pressure. *Am Miner* 97:1749–1763
- Hochella M, Brown G, Ross F, Gibbs G (1979) High temperature crystal chemistry of hydrous Mg- and Fe-cordierites. *Am Miner* 64:337–351
- Ikawa H, Otagiri T, Imai O, Suzuki M, Urabe K, Udagawa S (1986) Crystal structures and mechanism of thermal expansion of high cordierite and its solid solutions. *J Am Ceram Soc* 69:492–498
- Kaindl R, Tropper P, Deibl I (2006) A semiquantitative technique for determination of CO₂ in cordierite by Raman spectroscopy in thin sections. *Eur J Miner* 18:331–335
- Kaindl R, Töbrens D, Haefeker U (2011) Quantum-mechanical calculations of the Raman spectra of Mg- and Fe-cordierite. *Am Miner* 96:1568–1574
- Kolesov BA (2006) Raman spectra of single H₂O molecules isolated in cavities of crystals. *J Struct Chem* 47:21–34
- Kolesov A, Geiger CA (2000) Cordierite II. The role of CO₂ and H₂O. *Am Miner* 85:1265–1274
- Langer K, Schreyer W (1976) Apparent effects of molecular water on the lattice geometry of cordierite: a discussion. *Am Miner* 61:1036–1040
- Lee WE, Mitchell TE, Heuer AH (1986) Electron beam-induced phase decomposition of cordierite and enstatite. *Radiat Eff* 97:115–126
- Likhacheva AY, Goryainov SV, Krylov AS, Bul'bak TA, Prasad PSR (2012) Raman spectroscopy of natural cordierite at high water pressure up to 5 GPa. *J Raman Spectros* 43:559–563
- Likhacheva AY, Goryainov SV, Bul'bak TA (2013) An X-ray diffraction study of the pressure-induced hydration in cordierite at 4–5 GPa. *Am Miner* 98:181–186
- Malcherek T, Domeneghetti MC, Tazzoli V, Ottolini L, McCammon C, Carpenter MA (2001) Structural properties of ferromagnesian cordierites. *Am Miner* 86:66–79
- Mao HK, Xu J, Bell PM (1986) Calibration of the ruby pressure scale to 800 kbars under quasi-hydrostatic conditions. *J Geophys Res* 9:4673–4676
- McMillan P, Putnis A, Carpenter MA (1984) A Raman spectroscopic study of Al-Si ordering in synthetic magnesium cordierite. *Phys Chem Miner* 10:256–260
- Miletich R, Reifler H, Kunz M (1999) The “ETH diamond-anvil cell” design for single-crystal XRD at non-ambient conditions. *Acta Crystallogr A55*: Abstr. P08.CC.001
- Miletich R, Allan DR, Kuhs WF (2000) High-pressure single-crystal techniques. In Hazen RM (ed) High-temperature and high-pressure crystal chemistry. *Rev Miner Geochem* 41:445–520
- Miletich R, Gatta GD, Redhammer GJ, Burchard M, Meyer HP, Weikusat C, Rotiroti N, Glasmacher UA, Trautmann C, Neumann R (2010) Structure alterations in microporous (Mg, Fe)₂Al₄Si₅O₁₈ crystals induced by energetic heavy-ion irradiation. *J Solid State Chem* 183:2372–2381
- Miletich R, Gatta GD, Willi T, Mirwald PW, Lotti P, Merlini M, Rotiroti N, Loerting T (2014) Cordierite under hydrostatic compression: anomalous elastic behaviour as a precursor for a pressure-induced phase transition. *Am Miner* 99:479–493
- Miro S, Grebille D, Chateigner D, Pelloquin D, Stoquert J-P, Grob J-J, Costantini J-M, Studer F (2005) X-ray diffraction study of damage induced by swift heavy ion irradiation in fluorapatite. *Nucl Instrum Meth Phys Res B* 227:306–318
- Mirwald PW (1981) Thermal expansion of anhydrous Mg-cordierite between 25 and 900 °C. *Phys Chem Miner* 7:268–270
- Nasdala L, Wildner M, Wirth R, Groschopf N, Pal DC, Möller A (2006) Alpha particle haloes in chlorite and cordierite. *Mineral Petrol* 86:1–27
- Putnis A (1980a) Order-modulated structures and the thermodynamics of cordierite reactions. *Nature* 287:128–131
- Putnis A (1980b) The distortion index in anhydrous Mg cordierite. *Contrib Mineral Petrol* 74:135–141
- Ramos SMM, Clerc C, Canut B, Chaumont J, Toulemonde M, Bernas H (2000) Damage kinetics in MeV gold ion-irradiated crystalline quartz. *Nucl Instrum Meth Phys Res B* 31:166–167
- Redfern SAT, Salje EKH, Maresch W, Schreyer W (1989) X-ray powder diffraction and infrared study of the hexagonal to orthorhombic phase transition in K-bearing cordierite. *Am Miner* 74:1293–1299
- Schouwink P, Miletich R, Ullrich A, Glasmacher U, Trautmann C, Neumann R, Kohn B (2010) Ion tracks in apatite at high pressures: the effect of crystallographic track orientation on the elastic properties of fluorapatite under hydrostatic compression. *Phys Chem Miner* 37:371–387
- Selkregg KR, Bloss FD (1980) Cordierites: compositional controls of Δ, cell parameters and optical properties. *Am Miner* 65:522–533
- Ullrich A, Schranz W, Miletich R (2009) The nonlinear anomalous lattice elasticity associated with the pressure-induced phase transition in spodumene: a high-precision static compression study. *Phys Chem Miner* 36:545–555
- Vetter J, Scholz R, Dobrev D, Nistor L (1998) HREM investigation of latent tracks in GeS and mica induced by high energy ions. *Nucl Instrum Meth Phys Res B* 141:747–752
- Wang SX, Wang LM, Ewing RC, Doremus RH (1998) Ion beam-induced amorphization in MgO–Al₂O₃–SiO₂. I. Experimental and theoretical basis. *J Non Cryst Solids* 238:198–213
- Weikusat C, Glasmacher UA, Miletich R, Neumann R, Trautmann C (2008) Raman spectroscopy of heavy ion induced damage in cordierite. *Nucl Instrum Meth Phys Res B* 266:2990–2993
- Weikusat C, Miletich R, Glasmacher UA, Trautmann C, Neumann R (2010) Heavy ion irradiation on crystallographically oriented cordierite and the conversion of molecular CO₂ to CO—a Raman spectroscopic study. *Phys Chem Miner* 37:417–424
- Ziegler JF, Biersack JP, Littmark U (1985) The stopping and range of ions in solids. Pergamon Press, New York, <http://www.srim.org/>